Scientia Iranica B (2023) 30(1), 77–89

Sharif University of Technology
Scientia Iranica
Transactions B: Mechanical Engineering
http://scientiairanica.sharif.edu

Research Note

Piezoelectric wind energy harvesting from vortex-induced vibrations of an elastic beam

A. Karimzadeh*, R. Roohi, and M. Akbari

Department of Mechanical Engineering, College of Engineering, Fasa University, Fasa, 74617-81189, Iran.

Received 10 January 2022; received in revised form 8 June 2022; accepted 1 October 2022

KEYWORDS
Piezoelectric energy harvester;
CFD simulation;
Vortex-Induced Vibration (VIV);
Elastic beam vibration;
Fluid-solid interaction.

Abstract. In the present study, the performance of a cylinder-based piezoelectric wind energy harvester attached to an elastic beam is numerically simulated. The wind flow perpendicular to the beam axis causes an oscillatory aerodynamic force exerted on the beam tip. The beam and the piezoelectric layer are modeled as elastic continuous bodies, and the continuum governing equations of the solid and piezoelectric layers are extracted. Moreover, the induced lift force by the vortex shedding downstream of the cylinder is estimated by the modified van der Pol wake oscillator equation. The cantilever mode shapes and the Galerkin method are applied to solve the three transient and coupled equations of elastic deflection, electrical resistance, and fluid force. Besides verifying the accuracy of the modified van der Pol equation, a moving object Computational Fluid Dynamics (CFD) simulation is also conducted. The effects of oscillator length, cylinder diameter, resistance load, structure and piezoelectric thickness as well as the wind speed on the produced power are investigated. According to the obtained results, upon increasing the cylinder diameter from 0.05 m by 100, 200, and 300%, the output power is increased by 219, 801, and 1502% at a wind speed of 5 m/s.

1. Introduction

Extraction of power from natural energy sources and application of the harvested energy in self-powered devices (e.g., Micro Electromechanical System (MEMS) sensors [1], pacemakers [2] and gyroscopes [3]) is an interesting topic for researchers [4,5]. Conversion of the ambient mechanical vibration into electrical power has drawn the highest attention due to its simplicity and availability. Therefore, energy harvesters based on piezoelectric [6–8], electrostatic [9], and electromagnetic [10] effects have been designed in recent years.

One of the newest and best methods for harvesting electrical energy from ambient vibrations is use of piezoelectric devices. Allen and Smits [11], for the first time, examined the vibration of piezoelectric membrane using the von Karman vortex street forming behind a bluff body. They studied the lock-in condition (when the frequency of the shedding vortices approaches the natural frequency of the solid structure) in the membrane. Wang and Ko [12] fabricated a piezoelectric energy harvester and analyzed the effects of piezoelectric film thickness and fluid pressure on the output voltage. They showed that their device could be integrated into pressure monitoring systems in tires or self-powering MEMS devices implanted in human bodies. Wang et al. [13] modeled, fabricated, and tested a Vortex-Induced Vibration (VIV) energy harvester prototype with electromagnetic induction for the first time. García Baena et al. [14] studied the

*. *Corresponding author.*
E-mail addresses: a-karimzadeh@fasau.ac.ir (A. Karimzadeh); Re.roohi@fasau.ac.ir (R. Roohi)

doi: 10.24200/sci.2022.59718.6393

vibration of a plate in the laminar wake behind a blunt body. They considered the vibrational mode shapes of the plate in their study. Wang et al. [15] analyzed a cantilever piezoelectric beam attached to a circular cylinder as a bluff body. They placed a rectangular plate downstream of the flow and studied the effect of the plate on the output voltage of the system. They also analyzed a high-performance piezoelectric wind energy harvester with Y-shaped attachments and illustrated that the Y-shaped attachments outperformed existing square attachments [16]. Zhang et al. [17] proposed a piezoelectric energy harvester for collecting rotational energy and developed a self-powered wireless sensor based on the proposed energy harvester.

The most piezoelectric VIV energy harvesters are designed based on an elastic base like beams and a bluff body such as circular cylinders to create vortices in the fluid flow. Barrero-Gil et al. [18] theoretically investigated a lumped model of VIV energy harvester. They studied the effect of mass ratio, mechanical damping, and the Reynolds number (Re) on the efficiency of the system and found that high efficiency values could be achieved at increased Re value. Akaydin et al. [19,20] implemented an elastic beam and circular cylinder inside a turbulent boundary layer parallel to the upstream flow. The aerodynamics, structural vibration, and electrical response as coupled phenomena were examined and the generated voltage and the device behavior for high Re were obtained, as well. Lai et al. [21] proposed a novel piezo-dielectric VIV energy harvester. They demonstrated that the generated power was higher than the PZT energy harvester. Zhao et al. [22] derived a closed-form solution for the coupled bending-torsion vibration of a VIV energy harvester.

Aerodynamic modeling of the vortices is one of the most important steps in designing and analyzing VIV energy harvesters. Dai and Abdelkefi [23] simulated the fluctuating lift coefficient by a van der Pol wake oscillator and coupled the lift equation with the deflection equation of the beam. They considered the base excitation and VIV on the system, in addition to the Ohm's law for the electrical formulation. Han et al. [24] investigated the vibration of the square section beam under flow using the van der Pol wake oscillator and lift equation and compared their results with the experimental data.

As is stated, the parametric study of these piezoelectric energy harvesters considering the coupled effect of continuous beam modeling, gauss electrical equation, and van der Pol lift equation simultaneously has not been performed earlier; therefore, in the present study, the performance of a piezoelectric VIV energy harvester is numerically examined to determine the effect of configuration and operational parameters on the harvested power. To do so, the governing equations including the beam deflection, the Gauss' law for piezoelectric electrical performance, and the modified van der Pol equation for the lift coefficient are solved simultaneously. Additionally, to verify the accuracy of the modified van der Pol equation, a moving object Computational Fluid Dynamics (CFD) simulation is also conducted based on the tip deflection of the examined beam. The effects of oscillator length, cylinder diameter, resistance load, structure and piezoelectric thickness, and the wind speed on the produced power are determined.

2. System modeling and governing equations

2.1. Beam vibration formulations

According to Figure 1 a bi-layered energy harvester cantilever beam with two isotropic elastic solid and piezoelectric layers is examined in the present study. The beam is subjected to a VIV force at its end due to

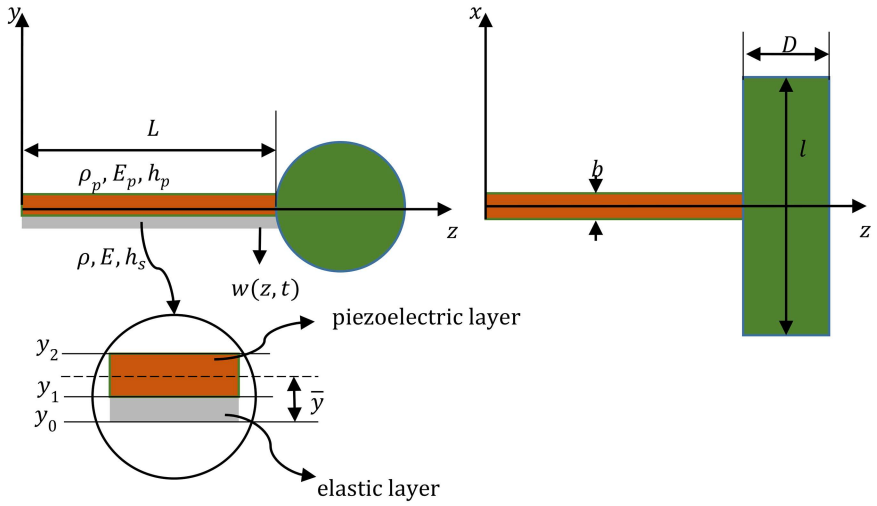

Figure 1. Schematics of the analyzed VIV energy harvester.

the presence of a cylinder with an axis perpendicular to the flow direction.

In order to obtain the system's governing equation of motion, the Hamilton principle is incorporated as:

$$\int_{t_1}^{t_2} \delta \left(W_e + T - U \right) dt = 0, \tag{1}$$

where T and U are the kinetic and strain energies, respectively, and W_e is the work done by the external force. The strain energy can be written as follows:

$$U = \frac{1}{2} \int_V \left(\sigma_{ij} + \sigma_{ij}^P \right) \varepsilon_{ij} dV, \tag{2}$$

where σ_{ij} and σ_{ij}^P are the stresses in the elastic solid and piezoelectric layers, respectively, and ε_{ij} is the infinitesimal strain in the structure. The non-zero component of the strain and corresponding stresses can be formulated as follows:

$$\varepsilon_{zz} = -y \frac{\partial^2 w}{\partial z^2}, \tag{3}$$

$$\sigma_{zz} = E \varepsilon_{zz}, \tag{4}$$

$$\sigma_{zz}^p = E_p \varepsilon_{zz} - e_{31} E_2 \left(t \right), \tag{5}$$

where E and E_p are Young's modulus of the elastic solid and piezoelectric layers in a constant electric field, $E_2 \left(t \right) = -\frac{V(t)}{h_p}$ is the electric field in the poling direction, $V \left(t \right)$ represents the voltage between the piezoelectric electrodes, and h_p is the piezoelectric layer thickness. Moreover, the kinetic energy and virtual work done by the external forces are obtained as follows:

$$T = \frac{1}{2} \int_0^L \left(\rho A + \rho_p A_p \right) \left(\frac{\partial w}{\partial t} \right)^2 dz, \tag{6}$$

$$\delta W_e = \left[F_{VIV} \delta \left(x - L \right) \right] \delta w, \tag{7}$$

where ρ, A, ρ_p, and A_p are density and cross-sectional area of the elastic and piezoelectric layers, respectively. Using the Hamilton's principle, the governing equations are derived in the following form:

$$E_T \frac{\partial^4 w}{\partial z^4} - \frac{1}{2} e_{31} b \left(y_1 + y_2 \right) V \left(t \right) \frac{d}{dz} \left(\delta \left(z \right) - \delta \left(z - L \right) \right) + \left(\rho A + \rho_p A_p \right) \frac{\partial^2 w}{\partial t^2} = F_{VIV} \delta \left(z - L \right). \tag{8}$$

It should be noted that F_{VIV} is the oscillating fluid force (which will be introduced in detail later) and δ is the Kronecker delta function. The corresponding boundary conditions are also obtained as:

$$w \left(0, t \right) = 0,$$

$$\frac{\partial w \left(0, t \right)}{\partial z} = 0,$$

$$\frac{\partial^2 w \left(L, t \right)}{\partial z^2} = 0,$$

$$\frac{\partial^3 w \left(L, t \right)}{\partial z^3} = 0, \tag{9}$$

where:

$$E_T = \frac{b}{3} \left(E \left(y_1^3 - y_0^3 \right) + E_p \left(y_2^3 - y_1^3 \right) \right), \tag{10}$$

where, according to Figure 1, the layer's position with respect to neutral axis is defined as follows:

$$\bar{y} = \frac{\left(h_p + h_s \right) E_p h_s}{2 \left(E_s h_s + E_p h_p \right)} + \frac{h_s}{2}, \tag{11}$$

$$y_0 = -\bar{y}, \quad y_1 = h_s - \bar{y}, \quad y_2 = h_s + h_p - \bar{y}. \tag{12}$$

The electric displacement D_e is related to the strain using:

$$D_e = e_{31} \varepsilon_{zz} + E_{33}^s E_2, \tag{13}$$

where E_{33}^s is the permittivity at constant strain. Given that the two electrodes are connected to external resistance R, with the implementation of the Gauss law, we have [25]:

$$-e_{31} b h_p \int_0^L \frac{\partial^3 w \left(z, t \right)}{\partial z^2 \partial t} dz - E_{33}^s \frac{bL}{h_p} \frac{dV}{dt} = \frac{V}{R}. \tag{14}$$

Moreover, to determine the time-dependent transverse load exerted on the cylinder due to the vortex induced fluctuations, the modified van der Pol equation is implemented as [26]:

$$\ddot{q} \left(t \right) - \varepsilon \Omega_f \left(q^2 - 1 \right) \dot{q} + \Omega_f^2 q = \frac{A}{D} \frac{\partial^2 w \left(L, t \right)}{\partial t^2}, \tag{15}$$

where q is the dimensionless fluctuation lift coefficient defined as $q \left(t \right) = \frac{2 C_L(t)}{C_{L0}}$, in which C_{L0} and $2 C_L \left(t \right)$ represent the lift coefficient for the fixed and vibrating cylinders, respectively. The magnitudes of A and ε can be determined based on the experimental examination of a rigid cylinder in forced vibration (the magnitudes of the utilized parameters are listed in Table 1). The vortex shedding frequency (Ω_f) is related to the free stream velocity (U_∞) and Strouhal number (S) as $\Omega_f = {2\pi S U_\infty}/{D}$. It should be noted that the right-hand side term represents the effect of body motion on the wake, while the negative linear ($-\varepsilon \Omega_f$) and nonlinear ($\varepsilon \Omega_f q^2$) damping terms ensure the amplitude increase at $q = 0$ and the saturation of q at $\ddot{z} = 0$, respectively.

Table 1. The list of the utilized parameters and constants as well as their benchmark magnitudes.

Parameter	Magnitude	Parameter	Magnitude
E_{33}^{s} (Fm^{-1})	1.328e-8	h_s(m)	1e-2
e_{31} (Cm^{-2})	–12.54	y_1 (m)	0.208e-2
ρ_p (kgm^{-3})	7800	y_2 (m)	1.208e-2
A_p (m^2)	1e-6	y_0 (m)	0.792e-2
C_{L0}	0.3	h_p (m)	1e-2
C_d	1.2	b(m)	1e-2
E_p (Nm^{-2})	66e9	R (Ω)	$10^4 - 10^7$
E (Nm^{-2})	193e9	Ω_f	1
D (m)	10e-2	ε	–
ρ (kgm^{-3})	8000	β	0.24
A (m^2)	1e-6	U_∞(ms^{-1})	1–6
L (m)	25e-2	–	–

The aerodynamic force (F_{VIV}) exerted on the fluctuating cylinder can be divided into drag and induced vortex forces that are formulated as follows:

$$F_{VIV} = \frac{\rho U_\infty^2 Dl}{2}\frac{C_{L0}q}{2} - \frac{\rho U_\infty Dl}{2}C_d\frac{\partial w(L,t)}{\partial t}, \quad (16)$$

where C_d and l are drag coefficient and length of the cylinder, respectively. Upon introducing the following dimensionless parameters, we have:

$$\hat{z} = \frac{z}{L}, \qquad \hat{w} = \frac{w}{L},$$

$$\hat{V} = \frac{1}{2}e_{31}b(y_1+y_2)\frac{L}{E_T}V,$$

$$\hat{F}_{VIV} = \frac{F_{VIV}L^2}{E_T} = \frac{\rho U Dl L^2}{2E_T}\left(U\frac{C_{L0}q}{2} - \frac{LC_d}{k}\frac{\partial\hat{w}(1,\hat{t})}{\partial\hat{t}}\right),$$

$$\hat{\Omega}_f = k\Omega_f, \qquad t = k\hat{t} = \left(\frac{(\rho A + \rho_p A_p)L^4}{E_T}\right)^{\frac{1}{2}}. \quad (17)$$

One can simply obtain the dimensionless governing equations by substitution of the dimensionless parameters (Eq. (17)) into Eqs. (8), (13), and (14) as follows:

$$\frac{\partial^4\hat{w}}{\partial\hat{z}^4} - \hat{V}(\delta'(\hat{z}) - \delta'(\hat{z}-1)) + \frac{\partial^2\hat{w}}{\partial\hat{t}^2} = \hat{F}_{VIV}\delta(\hat{z}-1), \quad (18)$$

$$\alpha\int_0^1 \frac{\partial^3\hat{w}}{\partial\hat{z}^2\partial\hat{t}}d\hat{z} - \frac{d\hat{V}}{d\hat{t}} = \gamma\hat{V}, \quad (19)$$

$$\frac{\partial^2 q}{\partial\hat{t}^2} - \varepsilon\hat{\Omega}_f(q^2-1)\frac{\partial q}{\partial\hat{t}} + \hat{\Omega}_f^2 q = \frac{AL}{D}\frac{\partial^2\hat{w}(1,\hat{t})}{\partial\hat{t}^2}, \quad (20)$$

in which:

$$\alpha = -\frac{e_{31}bh_p(y_1+y_2)}{2E_T E_{33}^s}, \qquad \gamma = -\frac{kh_p}{E_{33}^s bLR}. \quad (21)$$

The beam deflection can be written in terms of the vibrational mode shapes of the cantilever beam [27].

$$\hat{w}(\hat{z},\hat{t}) = \sum_{j=1}^{n}\psi_j(\hat{z})\eta_j(\hat{t}), \quad (22)$$

where ψ is the vibrational mode shape of the beam and the first mode shape is:

$$\psi_1(z) = \cos(\beta_1 z) - \cosh(\beta_1 z) - \frac{\cos(\beta_1)+\cosh(\beta_1)}{\sin(\beta_1)+\sinh(\beta_1)}(\sin(\beta_1 z) - \sinh(\beta_1 z)), \quad \beta_1 = 1.8751. \quad (23)$$

By using the first mode shape and the Galerkin approach, the three coupled governing equations can be rewritten as follows:

$$\eta_1\left(\int_0^1\psi_1^{(iv)}\psi_1 d\hat{z}\right) - \hat{V}\left(\int_0^1\psi_1(\delta'(\hat{z}) - \delta'(\hat{z}-1))d\hat{z}\right) + \frac{d^2\eta_1}{d\hat{t}^2}\left(\int_0^1\psi_1^2 d\hat{z}\right) = \hat{F}_{VIV}\left(\int_0^1\psi_1\delta(\hat{z}-1)d\hat{z}\right), \quad (24)$$

$$-\alpha\frac{d\eta_1}{d\hat{t}}\left(\int_0^1\psi_1''\hat{z}\right) - \frac{d\hat{V}}{d\hat{t}} = \gamma\hat{V}, \quad (25)$$

$$\frac{\partial^2 q}{\partial\hat{t}^2} - \varepsilon\hat{\Omega}_f(q^2-1)\frac{\partial q}{\partial\hat{t}} + \hat{\Omega}_f^2 q = \frac{AL}{D}\frac{d^2\eta_1}{d\hat{t}^2}\psi_1(1). \quad (26)$$

The parameters and constants as well as their benchmark magnitudes are listed in Table 1. Table 1 gives a list of the utilized parameters and constants as well as their benchmark magnitudes.

2.1.1. CFD simulation

The transient, 2D turbulent flow of the oscillating cylinder in the uniform flow is simulated using the CFD module of the COMSOL Multiphysics software. The implemented continuity and momentum equations (Navier-Stokes equations) are represented in Eqs. (27) and (28):

$$\frac{\partial\bar{u}_i}{\partial z_i} = 0, \quad (27)$$

$$\frac{\partial\bar{u}_i}{\partial t} + \bar{u}_j\frac{\partial\bar{u}_j}{\partial z_j} = -\frac{1}{\rho}\frac{\partial\bar{p}}{\partial z_j} + \frac{\mu}{\rho}\frac{\partial^2\bar{u}_i}{\partial z_i\partial z_j} - \frac{\partial}{\partial z_j}\overline{u_i' u_j'}, \quad (28)$$

where $\bar{u}_i$ and u_i' are the average and instantaneous components of the velocity field; μ and ρ are the fluid

viscosity and density; and $\overline{p}$ is the pressure field. To simulate the turbulent stress tensor (the last term on the right side of Eq. (27)), the standard $k-\varepsilon$ is utilized. It should be noted that several turbulence models are available in the literature; however, the standard $k-\epsilon$ model has been conventionally applied to the simulation of similar problems [28,29].

According to the standard $k-\varepsilon$ model, the turbulence stress tensor can be estimated via the solution of two coupled transport equations for kinetic energy and dissipation rate as follows:

$$\frac{\partial}{\partial t}(\rho k)+\frac{\partial}{\partial z_j}(\rho k\bar{u}_i)= \frac{\partial}{\partial z_j}\left(\mu+\frac{\mu_t}{\sigma_k}\frac{\partial k}{\partial z_j}\right) + G_k+G_b-\rho\varepsilon-Y_M+S_k, \tag{29}$$

$$\frac{\partial}{\partial t}(\rho\varepsilon)+\frac{\partial}{\partial z_j}(\rho\varepsilon\bar{u}_i) = \frac{\partial}{\partial z_j}\left(\mu+\frac{\mu_t}{\sigma_k}\frac{\partial\varepsilon}{\partial z_j}\right) + C_{1\varepsilon}\frac{\varepsilon}{k}(G_k+C_{3\varepsilon}G_b)-C_{2\varepsilon}\rho\frac{\varepsilon^2}{k}+S_\varepsilon, \tag{30}$$

where the constant parameters in Eqs. (24) and (25) are assumed to have the following magnitudes:

$$\sigma_\varepsilon=1.3,\quad \sigma_k=1,\quad C_{1\varepsilon}=1.44,\quad C_{2\varepsilon}=1.44. \tag{31}$$

The turbulence viscosity (μ_t) in Eqs. (29) and (30) is determined based on the obtained values for the kinetic energy and dissipation rate at each computational grid according to Eq. (32) as:

$$\mu_t=\rho C_\mu\frac{k^2}{\varepsilon}. \tag{32}$$

3. Solution method

The three (elastic solid, electrical, and fluid) coupled time-dependent equations are solved with MATLAB software numerically. This solution is obtained using MATLAB's ODE23s function for the ordinary differential equation (where ODE23s is on the basis of the integration method, Runge Kutta23). Based on the extracted mechanical and electrical responses, the time-dependent behavior of the system is analyzed in the following section.

4. Results and discussion

4.1. Validation

4.1.1. Solid and piezoelectric equations

By replacing the vortex induced force by a harmonic excitation in Eq. (24) and ignoring the lift coefficient equation (Eq. (26)), the steady-state response of the energy harvester can be derived analytically.

$$a_1\eta_1+a_2\hat{V}+a_3\frac{d^2\eta_1}{d\hat{t}^2}=F_e\sin\left(\Omega_e\hat{t}\right), \tag{33}$$

$$a_4\frac{d\eta_1}{d\hat{t}}-\frac{d\hat{V}}{d\hat{t}}-\gamma\hat{V}=0, \tag{34}$$

where:

$$a_1=\int_0^1\psi_1^{(iv)}\psi_1 d\hat{z},$$

$$a_2=\int_0^1\psi_1\left(\delta'(\hat{z})-\delta'(\hat{z}-1)\right)d\hat{z},$$

$$a_3=\int_0^1\psi_1^2 d\hat{z},$$

$$a_4=-\alpha\left(\int_0^1\psi_1''\hat{z}\right), \tag{35}$$

where F_e and Ω_e are the dimensionless amplitude and frequency of the assumed tip harmonic force, respectively. The following form is considered as the response of Eqs. (24) and (25).

$$\eta\left(\hat{t}\right)=a_{01}\sin\left(\Omega_e\hat{t}\right)+a_{02}\cos\left(\Omega_e\hat{t}\right), \tag{36}$$

$$\hat{V}\left(\hat{t}\right)=b_{01}\sin\left(\Omega_e\hat{t}\right)+b_{02}\cos\left(\Omega_e\hat{t}\right). \tag{37}$$

By inserting the above equations into Eqs. (24) and (25) and solving the obtained algebraic equations, the analytical solution of the unknown parameters can be expressed as follows:

$$a_{01}=\frac{\left(a_1\gamma^2+\left(a_1+a_2a_4-a_3\gamma^2-a_3\Omega_e^2\right)\Omega_e^2\right)F_e}{\Delta},$$

$$a_{02}=\frac{\left(a_2a_4\gamma\Omega_e\right)F_e}{\Delta},$$

$$b_{01}=\frac{\left(a_1a_4+a_2a_4^2-a_3a_4\Omega_e^2\right)\Omega_e^2F_e}{\Delta},$$

$$b_{02}=\frac{\left(a_1a_4-a_3a_4\Omega_e^2\right)\gamma\Omega_eF_e}{\Delta},$$

$$\Delta=a_1^2\gamma^2+(a_1^2+2a_1a_2a_4+a_2^2a_4^2-2a_1a_3\gamma^2)\Omega_e^2+(2a_1a_3-2a_2a_3a_4+a_3^2\gamma^2)\Omega_e^4+a_3^2\Omega_e^6. \tag{38}$$

The time response of the tip deflection of the beam based on the analytical solution (Eqs. (36)–(38)) and the numerically obtained solution is illustrated in Figure 2. The numerical solution is in excellent agreement with the analytical response, which approved the accuracy of the numerical investigation presented in this study.

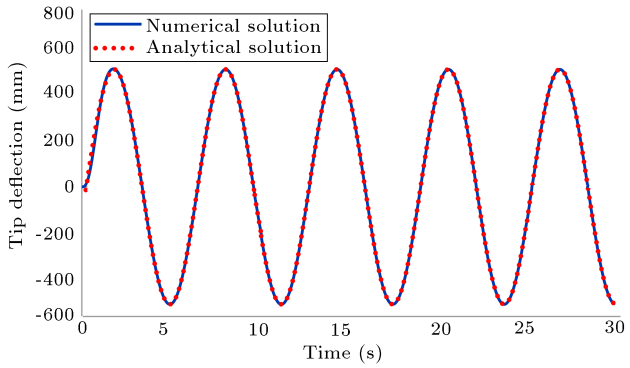

Figure 2. Numerical and analytical tip deflections $R = 1e^5\ \Omega$, $L = l = 25$ m, $F_e = 0.01$, $\Omega_e = 1$.

4.1.2. van der Pol equation

To verify the accuracy of the van der Pol equation, CFD simulation based on the obtained tip deflections is conducted. The cylinder diameter and the inlet velocity are set to 0.2 m and 5 m/s, respectively. The vertical motion of the cylinder, which is equal to the tip deflection, is extracted from the developed code and utilized as the mesh displacement in the COMSOL software settings. The variations of the lift force during the oscillations of the cylinder are calculated during the CFD simulation and compared with the implemented van der Pol equation.

The geometry and the boundary conditions are represented in Figure 3. The cylinder peripheral

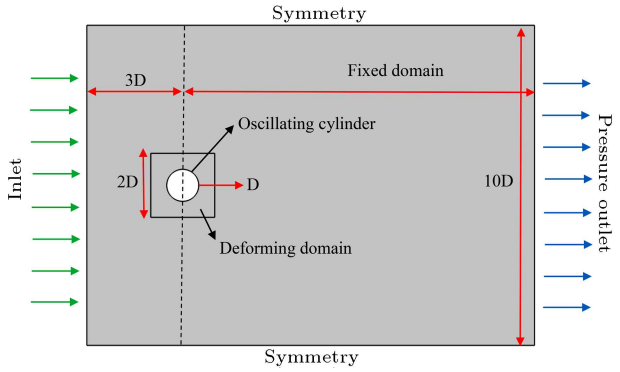

Figure 3. The geometry and boundary conditions used for CFD validation.

domain is extended sufficiently to increase the accuracy of the assigned boundary conditions. The flow field in the up and downstream is extended to 3 and 10 times of the cylinder diameter (D), while the upper and lower domain faces are set at a distance of 5D from the cylinder. To ensure the sufficiency of the computational domain dimensions, the deviation of the velocity and pressure variables on the horizontal and outlet surfaces from the assigned values at the boundaries is checked and verified.

An unstructured grid with six layers of body conforming meshes near the oscillating cylinder surface is utilized. To increase the simulation accuracy, the grids density near the cylinder is enhanced by reduction of the cells' sizing. The grid independency test is also conducted to determine the sufficient number of grid points with the optimum computational cost. To do so, four different computational grids with 40375 (coarse), 60986 (medium), 80758 (fine), and 105362 (very fine) cells are utilized; then, the variation in the lift coefficient value during one oscillating period is chosen as the decision criterion. The lift coefficient variation is illustrated in Figure 4. It is observed that the average difference between coarse and medium and that between medium and fine meshes are about 3.1 and 1.7%, respectively, while the same difference is reduced to 0.3% in comparison of the results of fine and very fine meshes. Therefore, to consider both of the accuracy and computational cost, the grid domain with 80758 cells is selected for CFD simulation.

The implemented tip deflection data are given in Figure 4. According to Figure 5, the tip deflection is increased non-linearly from zero to 0.51 μm in about 47.5 s and the periodic oscillation continues after that instance with the time period of 6.13 s. At the validation phase, only the periodic behavior with constant amplitude is incorporated and the initial amplitude growth phase is omitted from the CFD simulation.

The velocity magnitude contours at four time instances during one period of oscillations is revealed in Figure 6. The mentioned time period is selected after 15 oscillations to ensure the formation of periodic

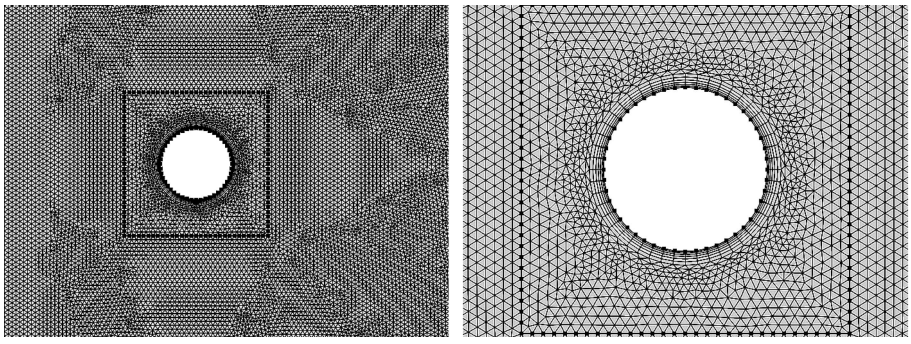

Figure 4. The implemented computational grids around the oscillating cylinder at two zoom levels.

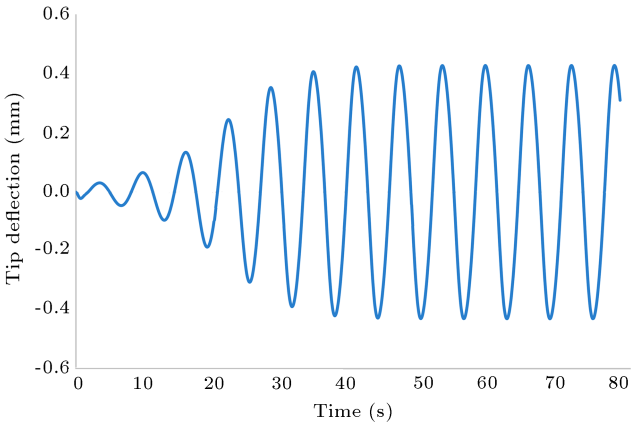

Figure 5. The implemented tip deflection data $R = 1e^5\ \Omega$, $D = 0.1$ m, $L = l = 25e^{-2}$ m.

behavior of the flow field. As it is obvious, even for the negligible amplitude of oscillations (i.e., 0.51 μm), due to the imposed wall velocity on the fluid, a vortex shedding pattern is created downstream of the cylinder. At $t = 0$ (t is measured from the initiation of an arbitrary cycle), a vortex starts to separate from the upper section and at $t = T/4$, it is completely detached, while the separation of the lower vortex begins at $t = T/2$. Therefore, during one oscillation, multiple vortexes are detached from the upper and lower sides of the cylinder with the direct influence of the pressure distribution on the cylinder and, consequently, the generated lift force. To examine the vortexes more clearly, the contours of the vortex magnitude is depicted in Figure 7.

The contours of vortex magnitude in the direction normal to the plane (z axis) are depicted in Figure 7. According to the results, the strength of the detached vortexes from the upper and lower sides of the cylinder is the same, but with the opposite rotational direction. The creation of the vortexes as well as their stretching and the detachment can be obviously observed in Figure 7(a) to (d). Therefore, during each oscillation cycle, ascending and descending behaviors for the lift coefficient are predictable, as discussed in Figure 8.

The lift coefficient obtained from the van der Pol equation is compared with the CFD modeling in Figure 7(b). Based on the obtained results, it is observed that an average difference of 6.7% exists between two sets of data. Regarding the level of simplification of the van der Pol equation besides the significant reduction of the computational cost by implementation of the van der Pol equation, the utilization of this equation for lift evaluation is verified. However, it should be added that the validation is also conducted for other cases of operational conditions and similar deviation from the CFD results is observed.

4.2. The effect of cylinder diameter

According to the obtained results, the effect of cylinder diameter and length on the harvested power is non-

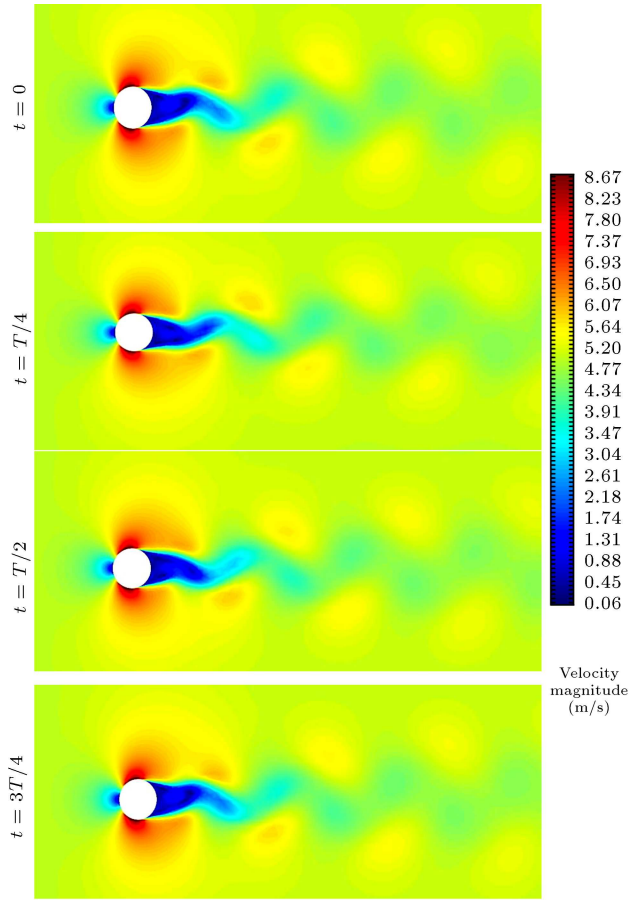

Figure 6. The velocity magnitude contours and the vortex street pattern at various time instances during one oscillation cycle (T: Oscillation time period).

linear and more pronounced for larger cylinders. In other words, by increasing the cylinder diameter from 0.05 m by 100, 200, and 300%, the output power is increased by 219, 801, and 1502% at a wind speed of 5 m/s, respectively (see Figure 9).

The beam deflection is also growing with an increase of the cylinder diameter; however, the relative amount of increase in the tip deflection is lower than the power enhancement percentage (Figure 10). At a wind speed of 5 m/s, by increasing the diameter by 100, 200, and 300%, the tip deflect growth is calculated to be 85.2, 199.5, and 299.4%. Therefore, it can be concluded that at a wind speed of 5 m/s, the cylinder diameter has almost the same effect on the beam tip deflection. To justify the above finding, we should simply keep in mind that the increase in magnitude and frequency of the VIV force, which is dependent on the cylinder diameter and length, increases the tip deflection of the beam and the output power. However, increasing the VIV force would probably cause large deformations at the tip and more nonlinear behavior in beam deflection.

Investigation of the effect of cylinder diameter on output power for different rates of electrical load resistance reveals that the maximum gained power occurs

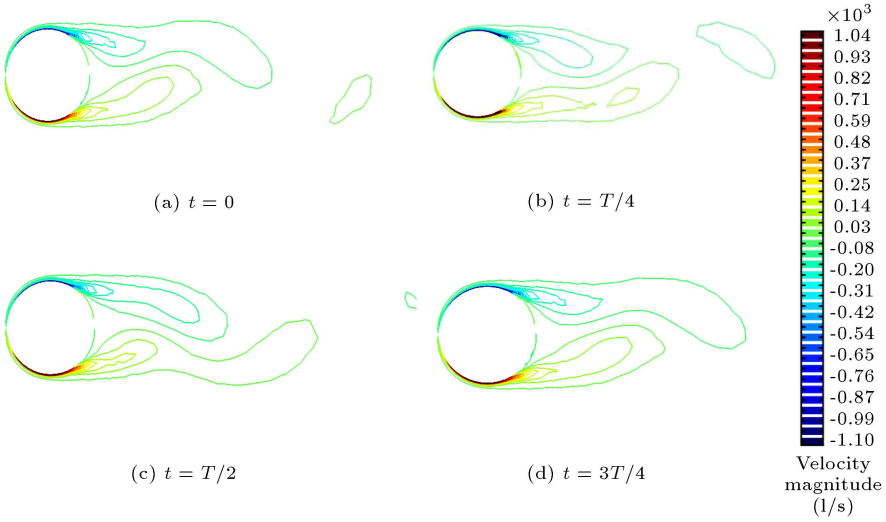

Figure 7. The evolution and separation of vortexes during one oscillation cycle (T: Oscillation time period).

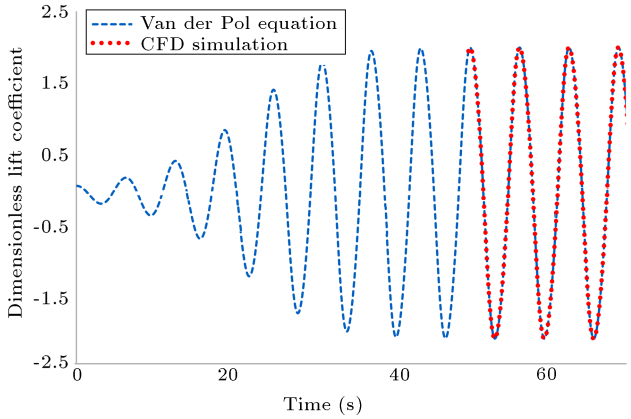

Figure 8. The comparison of the dimensionless lift coefficient between van der Pol equation and the CFD simulation ($R = 1e^5$ Ω, $D = 0.1$ m, $L = l = 25e^{-2}$ m).

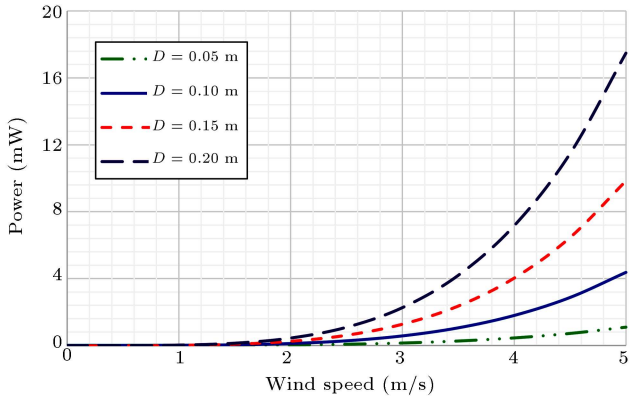

Figure 9. Effect of wind speed on the energy harvester output power ($R = 1e^5$ Ω, $L = l = 25e^{-2}$ m).

between 10^5 and 10^6 Ω for all the chosen diameters at a wind speed of 5 m/s (Figure 11). It should be added that the electrical load resistance is reported on a logarithmic scale for the horizontal axis. Therefore,

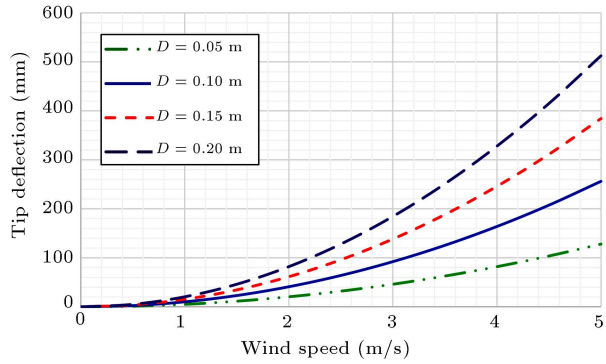

Figure 10. Effect of wind speed on beam tip deflection ($R = 1e^5$ Ω, $L = l = 25e^{-2}$ m).

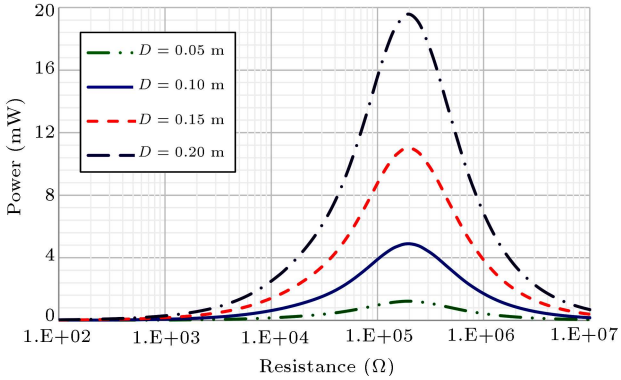

Figure 11. Energy harvester output power versus electrical load resistance for different cylinder diameters at the wind speed of ($U = 5\frac{m}{s}$, $L = l = 25e^{-2}$ m).

the output power around its extremum point (i.e., 200 kΩ) is very sensitive to the resistance load; however, at higher values of resistance, the harnessed power is reduced at a negligible slope and it can be said that the output power is almost independent from the load resistance for $R >> 200$ kΩ. From Eq. (16), the vortex

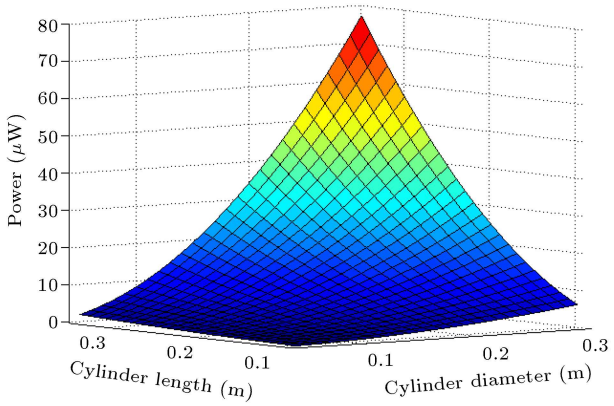

Figure 12. Effect of tip cylinder diameter and length on the energy harvester output power ($R = 1e^5$ Ω, $U = 5\frac{m}{s}$, $L = 25e^{-2}$ m).

shedding force is linearly dependent on the tip cylinder diameter; increase in the cylinder diameter raises the VIV force; and the output power increases given the increase in the cylinder diameter. However, given the nonlinear behavior of the device, the power increment is not linear.

Figure 12 shows the effect of cylinder diameter and length on the output power. Findings reveal that increasing the cylinder length improves the output power, as well. Therefore, one can design larger cylinders in length and diameter to obtain higher output powers for the examined VIV energy harvesters; however, the cost and occupation space limits and the power coefficients should be also considered for a precise design.

4.3. The effect of beam length

The beam length is another affecting parameter in the energy harvesting process of piezoelectric VIV. The output power for different beam lengths as well as electrical load resistance are plotted in Figure 13. It should be noted that the steel and piezoelectric layer lengths are considered to be equal in all the examined cases. Based on the obtained results, by increasing the beam length, the output power of the energy harvester is enhanced and it leads to a rise in the obtained voltage. Based on Figure 11, the maximum gained power occurs between the electrical resistance of 10^5 and 10^6 Ω; however, some major differences are observed upon comparing the behavior of output power in Figures 11 and 13. The maximum output power in Figure 11 occurs at constant load resistance (nearly at 200 kΩ), while the optimum power load resistance in Figure 13 changes by variation of the beam length. The mentioned behavior results from the direct effect of the beam length on the mechanical frequency of the system, which in turn affects the frequency of the separated vortexes and, consequently, shifts the value of the optimum electrical load resistance.

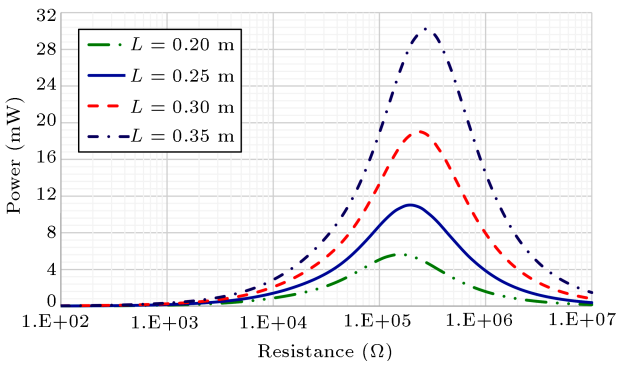

Figure 13. Output power versus electrical load resistance for different beam lengths ($U = 5\frac{m}{s}$, $D = 0.1$ m).

Based on the obtained results, it is revealed that by increasing the beam length from 0.2 to 0.35 m, the maximum output power increases from 5.64 to 30.2 μW and also the optimum resistance load grows from 158.4 to 281.3 kΩ. Therefore, via proper selection of the resistance load and the beam length, the output power significantly can be improved (e.g., in an optimum condition, 75% increase in the beam length results in a 435% enhancement in the harnessed energy). This finding helps researchers and designers adjust the PEH's frequency with the vortex shedding frequency to obtain maximum output power.

4.4. The effect of resistance load

The combined role of the beam length and load resistance in the energy harvester output power is depicted in Figure 14. As it is seen in Figure 14, increasing the beam length magnifies the output power; however, the growth pattern is not identical for all selected resistance rates. Based on Figure 13, it was concluded that the maximum output power was obtained between 10^5 and 10^6 Ω, as confirmed in Figure 14. For 10^5 Ω load resistance, increasing the beam length leads to higher power efficiency at a decreasing rate vs beam length, while for 10^6 Ω load resistance, increasing the beam length magnifies the power and its growth

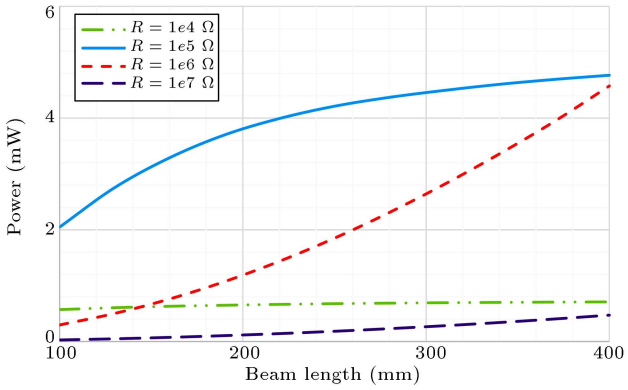

Figure 14. Energy harvester output power versus beam length for different electrical load resistance rates ($U = 5\frac{m}{s}$, $D = 0.1$ m, $l = 25e^{-2}$ m).

rate simultaneously. Besides, for 10^4 and 10^7 Ω rates of resistance, the variations of the beam length do not affect the output power significantly since the frequency of the vortex is close to the natural frequency of the device when the load resistance ranges between 10^5 and 10^6 Ω and much more power can be harvested at these load resistance rates.

4.5. The effect of wind speed

The beam tip deflection and VIV energy harvester output power versus wind speeds at four chosen load resistance rates are presented in Figures 15 and 16. Results indicate that higher wind speeds induce higher tip deflection and, consequently, higher output power at all load resistance rates. However, maximum tip deflection occurs at 10^4 Ω load resistance, while the maximum output power takes place at 10^5 Ω load resistance, which indicates that maximum deflection and power do not occur in the same operational conditions. Since the important parameter in the designing process of these energy harvesters is the output power and considering the aforementioned result, one can conclude that the 10^5 Ω load resistance should be used for these energy harvesters in the examined range of parameters.

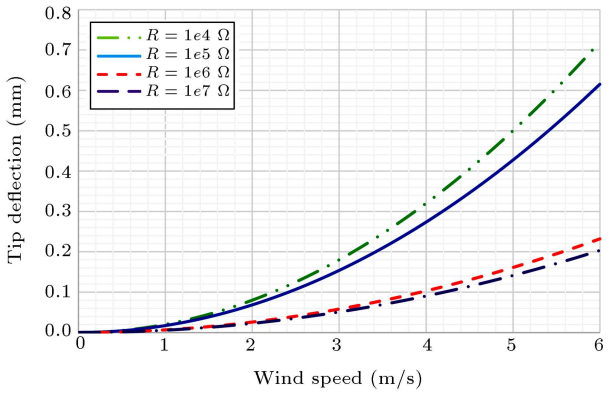

Figure 15. Energy harvester tip deflection versus wind speed for different electrical load resistance rates ($D = 0.1$, $L = l = 25e^{-2}$ m).

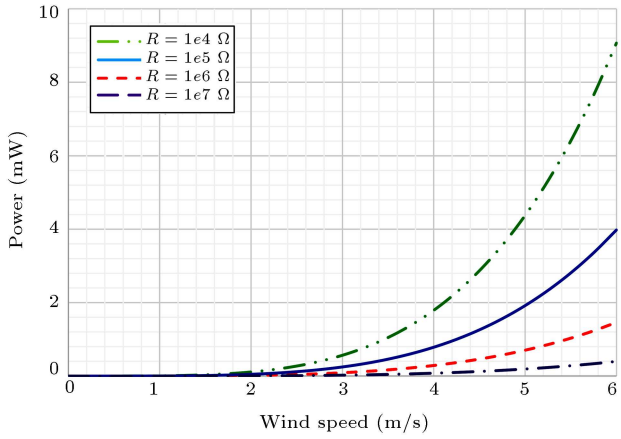

Figure 16. Energy harvester output power versus wind speed for different electrical load resistance rates ($D = 0.1$ m, $L = l = 25e^{-2}$ m).

Moreover, the enhancement of the beam stiffness due to the reverse piezoelectric effect is also evident according to the obtained tip deflection data. At a specific wind speed (which results in the same aerodynamic lift for constant beam length and cylinder diameter), the tip deflection is affected significantly via electrical resistance variations. Upon increasing the load resistance from 10^4 to 10^7 Ω, the tip deflection is reduced by 71.8% at a wind speed of 6 m/s. Moreover, it is observed that the stiffness of the beam is not affected significantly in the case of electrical resistances lower than 10^5 and higher than 10^6 Ω (due to the similarity of the deflection curves). Nonetheless, similar to the reported behaviors in Figures 12 and 13, the beam deflection is meaningfully affected in the range of 10^5 to 10^6 Ω.

Regarding the effect of wind speed on the performance of the harvesting system, it is observed that by increasing the wind speed from 2 to 4 and 6 m/s for 10^5 Ω cases, the output power grows by 1513 and 8062%, respectively (Figure 16). Therefore, the produced power is exponentially increased employing the piezoelectric harvester in regions receiving higher wind speeds.

4.6. The effect of piezoelectric and elastic layer thickness

The effect of the thickness of steel and piezoelectric layers on the energy harvester performance is illustrated in Figures 17 and 18. Following the reduction of the mentioned thickness, the harvester stiffness is lowered and the tip deflection is increased, which is favorable due to the enhancement of the output voltage and power. However, it should be mentioned that the results are valid until the basic assumptions of the simulation (Euler-Bernoulli beam assumption, small deformation in beams, etc.) are not violated.

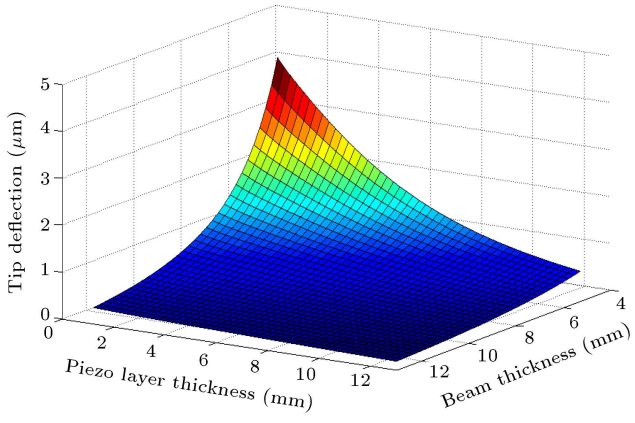

Figure 17. Energy harvester tip deflection versus beam and piezoelectric layers thickness ($U = 5\frac{m}{s}$, $R = 1e^5$ Ω, $D = 0.1$ m, $L = l = 25e^{-2}$ m).

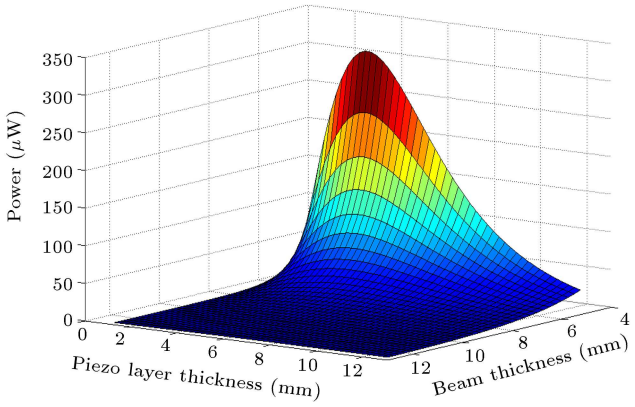

Figure 18. Energy harvester output power versus beam and piezoelectric layers thickness ($U = 5\frac{m}{s}$, $R = 1e^5$ Ω, $D = 0.1$ m, $L = l = 25e^{-2}$ m).

Figure 18 shows that the maximum output power is obtained when the steel and piezoelectric layers have close or, more precisely, exactly the same thicknesses. Findings also illustrate that as the steel layer is stiffer than the piezoelectric layer, any decrease in steel layer thickness places greater effect on the tip deflection and output power in comparison to the thickness of the piezoelectric layer. According to this figure, one can estimate that lowering the beam and piezo layer thickness increases the device deflection and output power, but decreasing the piezo layer thickness reduces the output power. Thus, the range of the optimum values for beam and piezo layer thicknesses should be derived.

5. Conclusion

The performance of piezoelectric Vortex-Induced Vibration (VIV) was examined, and the effects of configuration parameters (i.e., beam length, cylinder diameter, and layers' thickness) as well as operating conditions were investigated. Moreover, the variation of the output power as a function of wind velocity and electrical resistance was calculated. The obtained results can be briefed as follows:

1. As the cylinder diameter increased from the benchmark value of 0.05 m by 100, 200, and 300%, the generated power was enhanced by 219, 801, and 1502% at a wind speed of 5 m/s, respectively;
2. Examination of the effect of cylinder diameter on output power for different electrical load resistance rates reveals that the maximum gained power was achieved in the range of 10^5 to 10^6 Ω for all of the chosen diameters;
3. Based on the obtained results, it is observed that the enhancement of the beam length from 0.2 to 0.35 m leads to an enhancement in the maximum output power from 5.64 to 30.2 μW. Besides, the optimum resistance load grew from 158.4 to 281.3 kΩ through the mentioned beam enlargement;
4. By increasing the load resistance from 10^4 to 10^7 Ω, the tip deflection was reduced by 71.8% at the highest examined wind speed (i.e., 6 m/s);
5. According to the results, the reduction of the thickness of the steel and piezoelectric layers led to the lowering of the harvester stiffness and increase of the tip deflection, consequently. The mentioned growth in the vibration amplitude was significant due to the enhancement of the generated voltage and power;
6. Moreover, the comparison between the van der Pol equation predictions and dynamic mesh Computational Fluid Dynamics (CFD) simulation pointed to the average difference of 6.7% between two sets of data and, consequently, verified the utilization of the van der Pol equation.

Nomenclature

W_e	Work done by external forces
T	Kinetic energy
U	Strain energy
w	Beam transverse deflection
ε	Infinitesimal strain
σ	Stress in elastic solid
V	Voltage between the piezoelectric electrodes
E_p	Piezo Young's modulus
E	Elastic solid young modulus
E_2	Electric field in the poling direction
ρ	Elastic solid density
A	Elastic solid beam cross section area
h_p	Piezo layer density
A_p	Piezo layer cross section area
L	Cantilever beam length
z	Axial coordinate of the beam
y	Transverse coordinate of the beam
t	Time
F_{VIV}	Vortex-induced vibration force
E_{33}^s	Piezoelectric permittivity
$\bar{y}$	Neutral axis
h_p	Piezo layer thickness
h_s	Elastic layer thickness
b	Cantilever beam width
R	Load resistance
Ω_f	Vortex shedding frequency
q	Dimensionless fluctuation lift coefficient
U_∞	Free stream velocity

e_{31}	Piezoelectric coupling coefficient
C_{L0}	Lift coefficient for the fixed cylinder
C_d	Drag coefficient
D_e	Electric displacement vector
D	Cylinder diameter
l	Cylinder length

References

1. Le Scornec, J., Guiffard, B., Seveno, R., et al. "Self-powered communicating wireless sensor with flexible aero-piezoelectric energy harvester", *Renew. Energ.*, **184**, pp. 551–563 (2022).
2. Azimi, S., Golabchi, A., Nekookar, A., et al. "Self-powered cardiac pacemaker by piezoelectric polymer nanogenerator implant", *Nano Energy.*, **83**, pp. 105781 (2021).
3. Karimzadeh, A. and Ahmadian, M.T. "Vibrational characteristics of size-dependent vibrating ring gyroscope", *Sci. Iran.*, **25**(6): Special Issue Dedicated to Professor Goodarz Ahmadi, pp. 3151–3160 (2018).
4. Wang, J., Geng, L., Ding, L., et al. "The state-of-the-art review on energy harvesting from flow-induced vibrations", *Appl. Energ.*, **267**, 114902 (2020).
5. Wiriyasart, S. and Naphon, P. "Thermal to electrical closed-loop thermoelectric generator with compact heat sink modules", *Int. J. Heat Mass Tran.*, **164**, 120562 (2021).
6. Eugeni, M., Elahi, H., Fune, F., et al. "Numerical and experimental investigation of piezoelectric energy harvester based on flag-flutter", *Aerosp. Sci. Technol.*, **97**, 105634 (2020).
7. Akkaya Oy, S. "A design of mass-spring type piezoelectric energy harvesting", *Sci. Iran.*, **28**(6), pp. 3504–3511 (2021).
8. Zhang, L., Xu, X., Han, Q., et al. "Energy harvesting of beam vibration based on piezoelectric stacks", *Smart Mater. Struct.*, **28**(12), 125020 (2019).
9. Hassena, M.A.B., Samaali, H., Ouakad, H.M., et al. "2D electrostatic energy harvesting device using a single shallow arched microbeam", *Int. J. NonLin. Mech.*, **132**, 103700 (2021).
10. Yan, B., Yu, N., Zhang, L., et al. "Scavenging vibrational energy with a novel bistable electromagnetic energy harvester", *Smart Mater. Struct.*, **29**(2), 025022 (2020).
11. Allen, J.J. and Smits, A.J. "Energy harvesting eel", *J. Fluid. Struct.*, **15**(3–4), pp. 629–640 (2001).
12. Wang, D.-A. and Ko, H.-H. "Piezoelectric energy harvesting from flow-induced vibration", *J. Micromech. Microeng.*, **20**(2), 025019 (2010).
13. Wang, D.-A., Chiu, C.-Y., and Pham, H.-T. "Electromagnetic energy harvesting from vibrations induced by Kármán vortex street", *Mechatronics.*, **22**(6), pp. 746–756 (2012).
14. García-Baena, C., Jiménez-González, J.I., Gutiérrez-Montes, C., et al. "Numerical analysis of the flow-induced vibrations in the laminar wake behind a blunt body with rear flexible cavities", *J. Fluid. Struct.*, **100**, 103194 (2021).
15. Wang, J., Zhang, C., Zhang, M., et al. "Enhancing energy harvesting from flow-induced vibrations of a circular cylinder using a downstream rectangular plate: An experimental study", *Int. J. Mech. Sci.*, **211**, 106781 (2021).
16. Wang, J., Zhou, S., Zhang, Z., et al. "High-performance piezoelectric wind energy harvester with Y-shaped attachments", *Energ. Convers. Manage.*, **181**, pp. 645–652 (2019).
17. Zhang, L., Zhang, F., Qin, Z., et al. "Piezoelectric energy harvester for rolling bearings with capability of self-powered condition monitoring", *Energy.*, **238**, 121770 (2022).
18. Barrero-Gil, A., Pindado, S., and Avila, S. "Extracting energy from vortex-induced vibrations: a parametric study", *Appl. Math. Model.*, **36**(7), pp. 3153–3160 (2012).
19. Akaydin, H.D., Elvin, N., and Andreopoulos, Y. "Energy harvesting from highly unsteady fluid flows using piezoelectric materials", *J. Intel. Mat. Syst. Str.*, **21**(13), pp. 1263–1278 (2010).
20. Akaydın, H.D., Elvin, N., and Andreopoulos, Y. "Wake of a cylinder: a paradigm for energy harvesting with piezoelectric materials", *Exp. Fluids.*, **49**(1), pp. 291–304 (2010).
21. Lai, Z., Wang, S., Zhu, L., et al. "A hybrid piezo-dielectric wind energy harvester for high-performance vortex-induced vibration energy harvesting", *Mech. Syst. Signal Pr.*, **150**, p. 107212 (2021).
22. Zhao, X., Zhu, W.D., and Li, Y.H. "Closed-form solutions of bending-torsion coupled forced vibrations of a piezoelectric energy harvester under a fluid vortex", *J. Vib. Acoust.*, **144**(2) (2022).
23. Dai, H.L., Abdelkefi, A., and Wang, L. "Piezoelectric energy harvesting from concurrent vortex-induced vibrations and base excitations", *Nonlinear Dynam.*, **77**(3), pp. 967–981 (2014).
24. Han P, Hémon P, Pan G, et al. "Nonlinear modeling of combined galloping and vortex-induced vibration of square sections under flow", *Nonlinear Dynam.*, **103**(4), pp. 3113–3125 (2021).
25. Abdelkefi, A., Najar, F., Nayfeh, A.H., et al. "An energy harvester using piezoelectric cantilever beams undergoing coupled bending-torsion vibrations", *Smart Mater. Struct.*, **20**(11), 115007 (2011).
26. Facchinetti, M.L., De Langre, E., and Biolley, F. "Coupling of structure and wake oscillators in vortex-induced vibrations", *J. Fluid. Struct.*, **19**(2), pp. 123–140 (2004).
27. Rao, S.S., *Vibration of Continuous Systems*, John Wiley & Sons (2019).

28. Coughtrie, A.R., Borman, D.J., and Sleigh, P.A. "Effects of turbulence modelling on prediction of flow characteristics in a bench-scale anaerobic gas-lift digester", *Bioresource Technol.*, **138**, pp. 297–306 (2013).

29. Jain, R. and Mohammad, U. "CFD approach of Joukowski airfoil ($T = 12\%$), comparison of its aerodynamic performance with NACA airfoils using k-ŏ3b5 turbulence model with 3 million Reynolds number", *Int. Res. J. Eng. Technol.*, **5**(10), pp. 1414–1418 (2018).

Biographies

Ali Karimzadeh was born in 1988. He received the BS degree in Mechanical Engineering from the Shiraz University in 2010 and the MS degree in Mechanical Engineering from the Sharif University of Technology in 2012 in Tehran. He received a PhD degree from the Department of Mechanical Engineering at the Sharif University of Technology in 2018. He has started working as an Assistant Professor at Fasa University from 2018. His research interests are in the areas of micro electromechanical systems, strength of material, advanced finite-element method, and non-classical continuum theories.

Reza Roohi was born in 1986. He received the BS degree in Mechanical Engineering from the Shiraz University in 2008 and the MS degree in Mechanical Engineering from Shiraz University in 2010 in Shiraz. He received a PhD degree from the Department of Mechanical Engineering at Shiraz University in 2016. He has started working as an Assistant Professor at Fasa University from 2018. His research interests are in the areas of computational fluid dynamic, biomechanics, and novel renewable energy systems.

Masoud Akbari was born in 1985. He received the BS degree in Mechanical Engineering from the Shiraz University in 2007 and the MS degree in Mechanical Engineering from the Shiraz University in 2009 in Shiraz. He received a PhD degree from the Department of Mechanical Engineering at the K.N.T.U in 2018. He has started working as an Assistant Professor at Fasa University from 2019. His research interests are in the areas of micro/nano electromechanical systems, and nano fluidic and renewable energy.